Materials Chemistry and Physics 115 (2009) 603–611

Contents lists available at ScienceDirect

Materials Chemistry and Physics

journal homepage: www.elsevier.com/locate/matchemphys

Morphology and texture of pulse plated zinc–cobalt alloy

M.S. Chandrasekar, Shanmugasigamani, Malathy Pushpavanam*

Central Electrochemical Research Institute, Karaikudi 630006, TN, India

ARTICLE INFO

Article history:
Received 18 August 2008
Received in revised form
19 November 2008
Accepted 8 January 2009

Keywords:
Alloy coatings
Microstructure
Electron microscopy (TEM and SEM)
Atomic force microscopy (AFM)

ABSTRACT

Pulse electrodeposition was used to produce zinc–cobalt (Zn–Co) alloy deposits from an alkaline non-cyanide electrolyte with and without additives. The influence of additives' concentration and pulse parameters, such as ON-time (T_{ON}), OFF-time (T_{OFF}), and pulse peak current density (I_P) on the surface morphology, grain size, composition and crystal orientation were investigated using scanning electron microscope (SEM), atomic forced microscope (AFM), energy dispersive X-ray (EDX), X-ray fluorescence (XRF), X-ray diffraction (XRD), respectively. At constant T_{OFF} and I_P, cobalt content in the deposits decreases with T_{ON} and cluster size increases. Increase in T_{OFF} at constant T_{ON} and I_P, decreases the cluster growth with increase in cobalt content. The same trend was observed with increasing I_P (without additives) at constant T_{ON} and T_{OFF}. The presence of additives at 7 Adm^{-2} drastically decreases the cobalt content in the deposits from 2.5 to 0.7 wt.%. Co and the preferred crystallographic orientation was [10.1] at 69.1% as confirmed by XRD.

1. Introduction

The application of sacrificial coatings of zinc onto steel and other ferrous substrates has long been established as an effective and reliable standard of the industry for corrosion protection. Recent demands for higher quality, mechanical property, corrosion resistant [1–6] and longer lasting finishes [7–12] have promoted a move to zinc alloy deposits especially in the fastener, electrical components, bicycle parts and aerospace. Toxic and environmentally harmful chromium and cadmium plating are being replaced by zinc alloy plating.

The differences in zinc alloys systems come from choice of alloying element and the electrolyte used as well. Successfully employed alloying elements are iron, cobalt, nickel and tin. The desired cobalt content of the alloy to achieve the above advantages is only 0.6–0.8 wt.% compared to zinc–nickel alloy requiring around 10–12 wt.% nickel [13–15].

Acidic [16–21] and alkaline [22,23] plating baths can be used for zinc and zinc alloy plating. Alkaline bath offers higher throwing power [7], produce single-phase zinc–nickel deposits and required less percentage of alloying elements (0.6–0.8 wt.% cobalt in zinc–cobalt and 10–12 wt.% Ni in zinc–nickel) for protective applications as compared to deposits obtained from acid baths (0.8–1.0 wt.% cobalt in zinc–cobalt and 14 wt.% nickel in zinc–nickel) [24]. Moreover, switching over from the existing neutral zinc plating to neutral zinc–cobalt alloy plating is very simple unlike the zinc–nickel system [25–30] due to lesser amount of cobalt and complexing agent required to obtain the desired composition compared to latter system. The operating conditions also are similar to zinc plating system in the former.

According to Brenner co-deposition of zinc with iron group metals follows the anomalous type in which the less noble metal (zinc) deposits preferentially under certain conditions [1]. Dahms and Croll [31] proposed the "hydroxide suppression mechanism" for nickel–iron alloys, suggested that the discharge of more noble Ni^{2+} ions is hindered by the formation of $Fe(OH)_2$ on the cathode surface, due to local pH rise, which inhibits the co-deposition of nickel. For zinc–cobalt alloy, Decroly and coworkers [32,33] and Higashi et al. [34,35] proposed that the discharge of Co^{2+} ions was hindered in the same manner by the formation of $Zn(OH)_2$ on cathode surface. Based on this theory, deposition conditions that can cause an increase in surface pH would enhance the anomalous co-deposition. However several reports disagree with latter mechanism [36,37]. Bahrololoom et al. [38] reported that the deposition mechanism changed from anomalous to equilibrium co-deposition and consequently high cobalt containing zinc–cobalt alloys were obtained if the Co^{3+} ions produced from anodic reaction were prevented from entering the catholyte.

The application of pulse current (PC) may be a possible approach to achieve zinc–cobalt alloys with a very wide range of alloy composition and properties by simply varying the applied pulse parameters such as ON-time (T_{ON}), OFF-time (T_{OFF}) and pulse peak current density (I_P). A qualitative review on pulse plating is elucidated in the literature [39]. In addition, the effect of pulse parameters and additives on the morphology, texture

* Corresponding author. Tel.: +91 4565 227550x227559; fax: +91 4565 227779x227713.
E-mail address: malathypush@yahoo.com (M. Pushpavanam).

0254-0584/$ – see front matter © 2009 Elsevier B.V. All rights reserved.
doi:10.1016/j.matchemphys.2009.01.020

and composition of zinc–cobalt is not exhaustively studied till date.

As a continuation of our earlier report on pulse electrodeposition of zinc from an alkaline non-cyanide bath [40], work on the production of zinc alloys was initiated from the same bath [41]. The present paper deals with zinc–cobalt alloy deposition using PC from the same bath using the same organic additives. The dependence of alloy composition, surface morphology, cathode current efficiency (CCE) and crystal orientations were studied as function of pulse parameters.

2. Experimental

2.1. Electrolyte and electrolytic cell

A zinc stock solution containing ZnO, 9–12 g l^{-1} (9–12 g l^{-1} Zn) and NaOH 90–120 g l^{-1} [40] was prepared with due pretreatments to remove the metallic and organic impurities [42,43]. Cobalt sulphate ($CoSO_4 \cdot 7H_2O$), 0.95–32 g l^{-1} (0.2–6.5 g l^{-1} cobalt) was mixed with 15–30 ml l^{-1} of triethanolamine (TEA) and made as a homogenous solution in order to avoid its precipitation in the alkaline medium. The pH of the electrolyte was 13–14. Required amount of cobalt solution was added to the zinc electrolyte before deposition. All chemicals used were of laboratory grade, supplied by Merck or Fischer.

Pulse electrodeposition was carried out in a 175 ml capacity cell. Mild steel plates were used as the cathode with an exposed area of 2 cm × 2 cm to obtain 5 μm thick zinc alloy deposit and (99.99% pure, Aldrich) zinc sheet as a soluble anode. Before electrodeposition, the steel plates were degreazed with trichloroethylene and given cathodic and anodic cleaning for 120 and 30 s, respectively in the conventional alkaline (cleaner) solution.

The experiments were carried out at 30–35 °C. The cathode current efficiency (%) was calculated from the mass gained after deposition [9].

2.2. Pulse electrodeposition

A DC regulated pulse power rectifier (Saral Systems, model: PR 1010 TPS, India) was used to generate the pulse waveforms. The effect of each pulse parameter on the deposit quality and properties was studied maintaining the other two constant. Coatings were obtained by varying T_{OFF} from 6 to 60.7 ms, T_{ON} from 6 to 15 ms and I_P from 2 to 13 Adm^{-2}. The effect of each pulse parameter on the deposit quality and properties was studied maintaining the other two at standard conditions: T_{OFF}, 21 ms; T_{ON}, 6 ms and I_P, 5 Adm^{-2}.

2.3. Characterization of zinc–cobalt deposits

The deposits were analyzed for their composition using X-ray fluorescence spectroscopy (CMI, XRX series, USA). A scanning electron microscope (SEM) (Hitachi, model: S3000H, Canada) together with energy dispersive X-ray (EDX) and atomic force microscope (AFM) (Molecular Imaging Scanning probe microscope, model: PICOSPM, US) were used to characterize the surface morphology of Zn–Co deposits. The grain size of Zn–Co platelet was calculated by averaging the length, width and thickness of each platelet observed and the root-mean-square (RMS) roughness (R_{RMS}) values were determined using AFM studies.

The electroplated sample was removed by washing with distilled water. The thin flakes floating in the water were then collected on to a copper grid. In this way the sample could be prepared just few minutes before loading in to transmission electron microscope (TEM). TEM images were collected from Philips CM200 microscope working at 200 kV.

X-ray diffraction (XRD) measurements were performed with X'pert PRO PANalytical (model: PW3040 160 X'pert PRO, Netherland) equipped with Cu Kα radiation. Crystal size was estimated by Scherrer's equation ($D = K\lambda/\beta\cos\theta$), where D is the crystal size, λ is the wavelength of the X-ray irradiation (1.5406 Å), K usually taken as 0.9, β is the full width half maximum (FWHM) of the diffraction peak and θ is the diffraction angle [44].

3. Results and discussion

3.1. Effect of bath composition on cobalt content in the alloy

The cobalt concentration in the alkaline electrolyte was varied from 2 to 45 wt.% Co, at constant 21 ms (T_{OFF}), 6 ms (T_{ON}) and 2 Adm^{-2} (I_P) (optimized DC current density [41] to obtain 0.5–0.8 wt.% Co content in the alloy). In Fig. 1, the cobalt content in the deposit is low initially and increased gradually with increase in cobalt concentration in the electrolyte. The CCE decreased from 90% at 7.65 wt.% Co to about 50% at 40.85 wt.% Co. At 7.65 wt.% cobalt in the electrolyte, optimum cobalt content was obtained and the same was used in the rest of the studies. It is understood that to produce an alloy deposit of the same cobalt content, less amount of cobalt in solution is required for PC than DC (9.4 wt.% Co [23,41]).

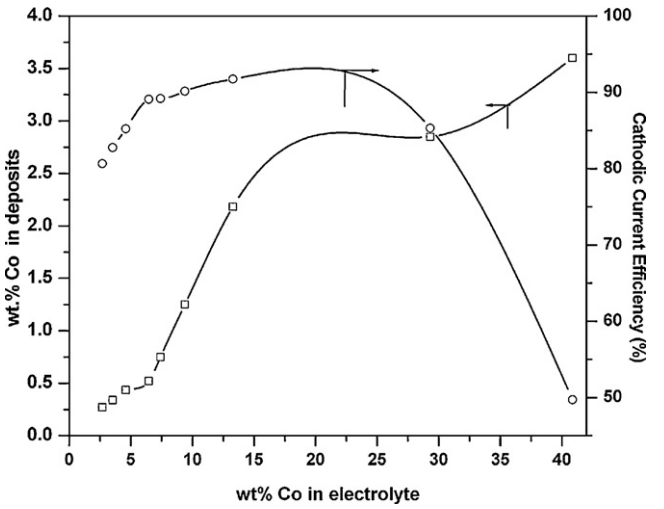

Fig. 1. Effect of cobalt concentration in the electrolyte on the cobalt content (wt.%) in the deposits and CCE (%) at constant 21 ms (T_{OFF}), 6 ms (T_{ON}) and 2 Adm^{-2} (I_P): (□) Wt.% Co; (○) CCE.

Figs. 2–4 show effect of each pulse parameter (T_{OFF}, T_{ON}, I_P) on the cobalt content in deposits and their corresponding CCE obtained from the optimized electrolyte (7.65 wt.% Co) while maintaining the other two constant. At constant 6 ms (T_{ON}) and 5 Adm^{-2} (I_P), the cobalt content in the deposit [23] increased from 3.5 to 4.5 wt.% with T_{OFF} while CCE decreased from 82 to 60% (Fig. 2). The cobalt content falls from 3.65 to 3.07 wt.% with increased T_{ON} at constant T_{OFF} (21 ms) and I_P (5 Adm^{-2}) but CCE increased from 78 to 84% (Fig. 3). At constant T_{ON} (6 ms), T_{OFF} (21 ms), the cobalt content increased with I_P and levels off above 11 Adm^{-2} irrespective of the additive's presence as shown in Fig. 4. Since the alloy deposition is decided by the surface pH, the cobalt content attains a peak at 5 Adm^{-2} itself whereas it is attained only at 11 Adm^{-2} at constant duty cycle (of 22.22%) (Fig. 4). The increase in cobalt content observed above 9 Adm^{-2} could be explained by the increase in partial current for cobalt deposition compared to that of zinc deposition.

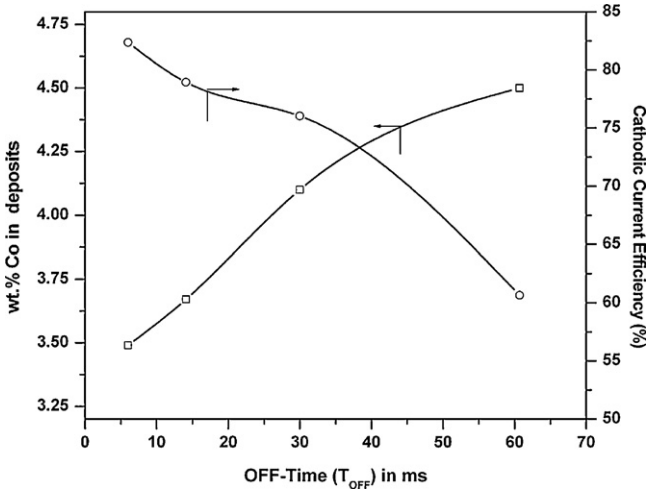

Fig. 2. Effect of T_{OFF} on the cobalt content (wt.%) in the deposits and corresponding CCE (%) at constant 6 ms (T_{ON}) and 5 Adm^{-2} (I_P). (Additive free electrolyte; Co in solution 7.65%.). (□) Wt.% Co; (○) CCE.

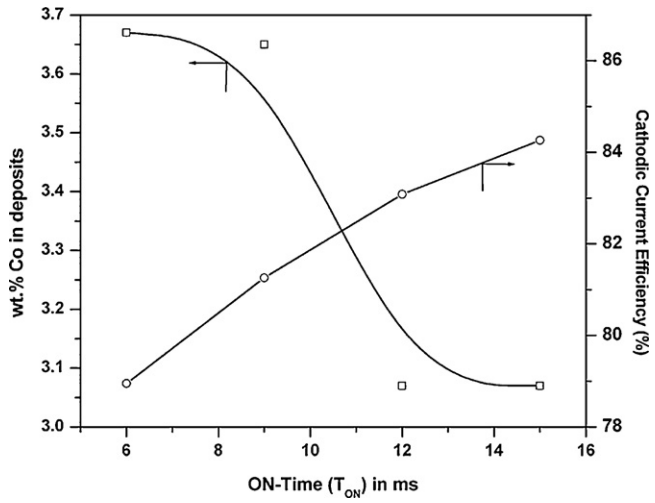

Fig. 3. Effect of T_{ON} on the cobalt content (wt.%) in the deposits and corresponding CCE (%) at constant 21 ms (T_{OFF}) and 5 Adm^{-2} (I_P). (Additive free electrolyte; Co in solution 7.65%). (□) Wt.% Co; (○) CCE.

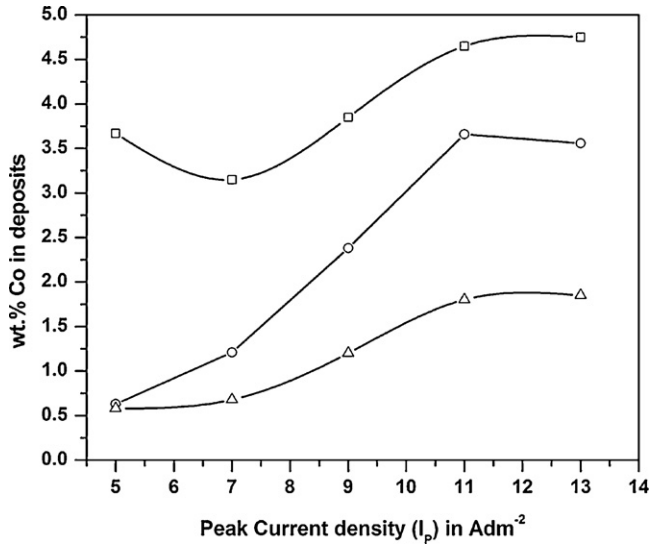

Fig. 4. Effect of I_P on the cobalt content (wt.% Co) in the deposits at constant 6 ms (T_{ON}) and 21 ms (T_{OFF}). (Co in solution 7.65%). (□) Without additive; (○) with PVA; (△) with PVA and PIP.

Deposits of 0.68–0.7 wt.% Co were obtained from electrolyte containing additives polyvinyl alcohol (PVA) and piperonal (PIP) at 5–7 Adm^{-2}. The organic additives inhibit deposition but, refine the grain size by specific adsorption onto the electrode surface.

All above results demonstrated anomalous deposition [1,45], in the sense that the cobalt content in the deposits was always less than the relative proportion present in the bath due to preferential deposition of less noble metal zinc. Stankeviciute et al. had reported that the "hydroxide suppression mechanism" to be a plausible explanation for latter since precipitation of scarcely soluble compounds during the current pulse take place. The decreased CCE during T_{OFF} increase had been attributed to the higher cobalt levels in the bath and deposit, which promote hydrogen-evolution reaction [45]. Ibl et al. had reported hydrogen is adsorbed during pulse T_{ON} and desorbed during T_{OFF}. When a new pulse comes, the surface is less covered with hydrogen and its deposition is facilitated, the result being lower CCE [46].

3.2. Morphology and topography

The nucleation rate is enhanced and the grain size of deposit is usually decreased because of higher I_P, however, the effect of T_{ON} and T_{OFF} on deposit characteristics cannot be predicted for certain systems, because the crystallization process is strongly influenced by adsorption and desorption phenomena. Therefore, each system may react differently during the electro-crystallization process yielding different surface morphology.

3.2.1. T_{OFF} effect

T_{OFF} is not a "dead" time from the standpoint of crystallization during which active center or recrystallization seems to takes place [47]. The fine-grained deposit obtained in practice depends upon what happens during the T_{OFF} period when the current is interrupted. Desorption of impurities and encouragement of renucleation with the formation of new, smaller grains can be allowed during this period [39]. Fig. 5a–c shows the SEM micrographs of deposits obtained at constant T_{ON} (6 ms), I_P (5 Adm^{-2}) and at various T_{OFF}. At 6 ms (T_{OFF}) (Fig. 5a), the deposit consisted of ~5–7 μm sized cauliflower-like clusters corresponding to quasi-pure cobalt deposits [1,9,48]. The micro-clusters were aggregates of cobalt nanoparticles (each sized ~45.7 nm) as analyzed by EDX. When T_{OFF} was increased from 21 to 30 ms, the micro-clusters diminished gradually forming modified stem-like dendrite deposit as shown in Fig. 5c. The increase in the T_{OFF} values caused the decrease in crystallites values from 7 to 2 μm and simultaneous slight decrease in grain size to 33.4 nm.

3.2.2. T_{ON} effect

Fig. 6 shows the SEM micrographs of deposits obtained at constant T_{OFF} (21 ms), I_P (5 Adm^{-2}) and at various T_{ON}. At 6 ms (T_{ON}), compact deposit with fewer interstices was obtained (Fig. 5b). With increased T_{ON} from 9 to 15 ms, Fig. 6a–c, the deposits obtained consisted of ~5–6 μm sized cauliflower-like micro-clusters. There were no appreciable decreases in cobalt content (3.65–3.07 wt.% Co) with

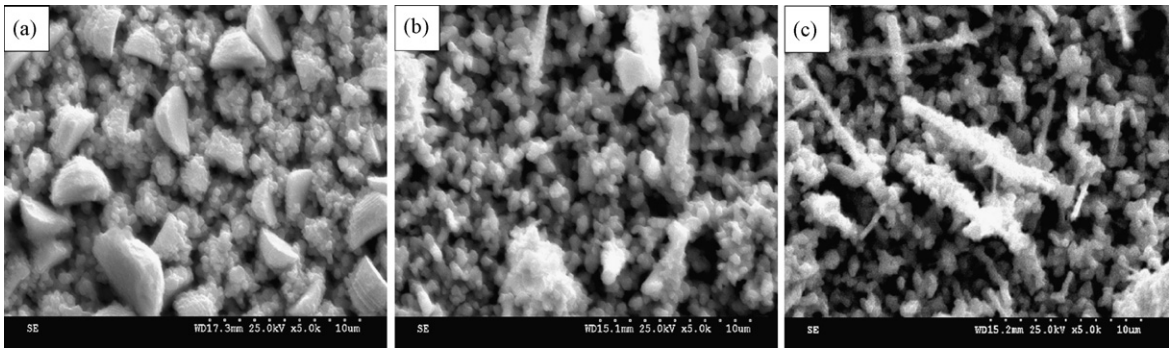

Fig. 5. SEM images of the surface morphology of zinc–cobalt deposits obtained at 6 ms (T_{ON}), 5 Adm^{-2} (I_P) and different OFF-time (T_{OFF}) of (a) 6 ms, (b) 21 ms, (c) 30 ms.

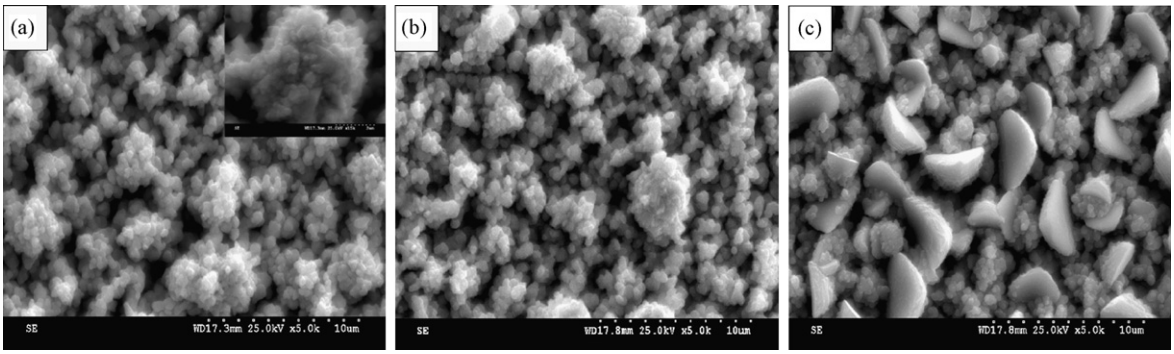

Fig. 6. SEM images of the surface morphology of zinc–cobalt deposits obtained at 21 ms (T_{OFF}), 5 Adm^{-2} (I_P) and different ON-time (T_{ON}) of (a) 9 ms (inset: 2 μm), (b) 12 ms, (c) 15 ms.

increase in T_{ON} values (Fig. 3). EDX analysis demonstrated that the clusters consisted of cobalt sized between 40 and 90 nm as shown in Fig. 6a (inset). The reappearance of the large crystallites at the longest T_{ON} (15 ms) may be explained by a large duty cycle value, which is approaching DC electrodeposition [27,49]. However, cluster deposits resembling Fig. 5a were obtained, which could be due to increased duty cycle (~42.86%).

3.2.3. I_P effect

Increase in the overpotential enhances the free energy to form new nuclei, which results in a higher nucleation rate and a smaller grain size. Therefore, an increase in I_P in the pulse plating of metals usually increases the overpotential that causes a decrease in the grain size. A similar effect was also observed for Zn–Co pulse electrodeposits [45].

3.2.3.1. Without additives. Fig. 7a–d shows the SEM micrographs of deposits obtained at constant T_{ON} (6 ms), T_{OFF} (21 ms) and at different I_P values. At 5 Adm^{-2}, the deposits of ~4–5 μm sized micro-clusters were obtained. When I_P increased to 11 Adm^{-2}, the former size gradually decreased to form compact deposits consisting of uniformly distributed clusters (~2–3.5 μm) Fig. 7b–d and AFM shows decrease in micro-cluster's size from 1.2 to 0.2 μm (Fig. 8a–d). Small particles of 20–80 nm collected together to form hemispherical (formed at 5–7 Adm^{-2}) and pyramidal (formed at 9–13 Adm^{-2}) cluster. The root-mean-square roughness of the deposits (260–210 nm) decreased with increase in I_P. The decrease in the size of grains was due to increase in overpotential that favors the nucleation process at the expense of the grain growth [50].

3.2.3.2. With PVA. Fig. 7e–h shows SEM micrographs of deposits obtained at 6 ms (T_{ON}), 21 ms (T_{OFF}), and at 5–13 Adm^{-2} (I_P). With 0.5 $g\,l^{-1}$ PVA inclusions, the deposits morphology changed enormously. The micro-clusters and interstices decreased (to ~1–2 μm) with increased I_P. The micro-cluster shape is gradually modified to compact deposits having less interstices and adherent prismatic platelets (Fig. 7 h). AFM studies depicted that deposits obtained at 5–9 Adm^{-2} consisted of micro-cluster containing 40–70 nm particles (Fig. 8e–f). Micro-cluster is formed by many 30–45 nm thick layers at higher I_P (Fig. 8g–h). RMS roughness increases (132–170 nm) with I_P, but comparatively less than the deposits obtained without additives. The ability of PVA to refine the grain size may be due to: (i) increasing the high overpotential and (ii) retardation of growth and increase in the effective nucleation rate [51].

3.2.3.3. With PVA and PIP. On addition of 0.2 $g\,l^{-1}$ PIP to the electrolyte containing 0.5 $g\,l^{-1}$ PVA, clustered deposits were not obtained. Instead, bright, compact, adherent deposits (~0.5–1 μm) with least interstices were obtained. The length of prismatic platelets size increased (300–550 nm) at higher I_P. The presence of 60 nm average-sized particles uniformly distributed over the latter is confirmed by AFM figures (Fig. 8i–l). The RMS roughness of the deposits decreased to ~100 nm comparative to deposits obtained with 0.5 $g\,l^{-1}$ PVA.

At 6 ms (T_{ON}), 21 ms (T_{OFF}) and 7 Adm^{-2} (I_P), TEM images confirm the existence of cobalt nanoparticles in the micro-cluster as shown in Fig. 9a. The presence of oxygen and cobalt in deposits are predicted by EDX (Fig. 9b). From EDX analysis, the deposit contained 0.68 wt.% Co. The ring pattern (Fig. 9c) obtained by using a selected area electron diffraction (SAED) aperture favoring many micro-crystallites diffraction [7]. The latter is shown in Fig. 9d that containing nanoparticles.

3.3. Phase composition

Zn–Co alloy coatings have the same structure as zinc deposits [52]. For accurate measurements of preferred orientations, area under each peak of the XRD patterns was determined. Relative texture co-efficient (RTC in %) for the reflections ($h\,k\,l$) were calculated by the formula [53]:

$$\text{RTC}\ (h\,k\,l) = \frac{(\text{TC}_{h\,k\,l})_E}{(TC_{h\,k\,l})_S} \times 100 \text{ and TC } (h\,k\,l) = \frac{(R_{h\,k\,l})_E}{(R_{h\,k\,l})_S}$$

Where TC, texture co-efficient of the planes ($h\,k\,l$); $R_{h\,k\,l}$, area under reflection intensity corresponding to ($h\,k\,l$) plane; E, sample under study; S, zinc powder sample to serve as a reference for the zinc samples.

3.3.1. T_{OFF} effect

Fig. 10 depicts T_{OFF} effect at constant T_{ON} (6 ms) and I_P (5 Adm^{-2}) on the lattice orientations of the Zn–Co deposits obtained. The micro-cluster depicted in SEM and AFM is in agreement with XRD that showed very sharp peaks characteristics of coarse grains. Considerable increases in the intensity of [10.1] peaks were observed when T_{OFF} increased from 6 to 60.7 ms while [00.2] and [10.0] showed no significant variation in intensity. This might be due to the change in orientation of the zinc crystallographic planes by the cobalt incorporation. The persistence of those peaks, although with less intensity, suggests the appearance of a zinc-rich (η-phase) Zn–Co alloy [54] since the diffraction pattern of the Zn–Co solid solution η-phase is very similar to pure zinc diffraction pattern [12]. The intensity of peak associated with cobalt hydroxide [$2\theta = 37.65^\circ$] (peak i) (JCPDS 45-0031] and cobalt oxide [$2\theta = 42.59^\circ$] (peak ii) (JCPDS 43-1004] increased with decrease in T_{OFF} followed by a decrease in intensity of [10.1] of the η-phase [54,55]. However, the basal [00.2] and pyramidal [10.1] peaks were dominant with increasing T_{OFF} that corresponds to the low overpotential [56,57]. With decrease in T_{OFF}, the peak associated with plane [10.1] shifted from 43.51° to 43.31° and for [00.2] from

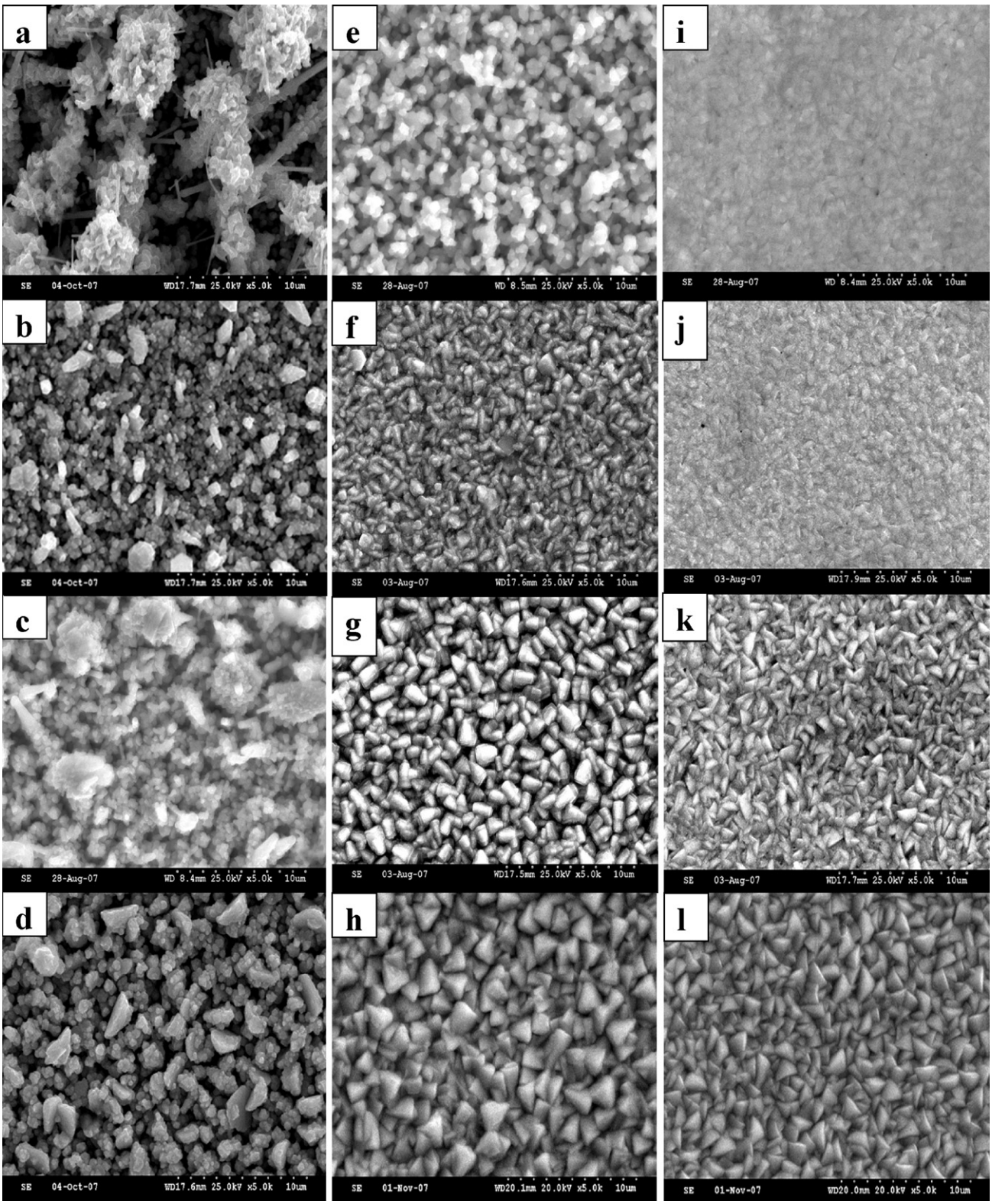

Fig. 7. SEM images of zinc–cobalt deposits obtained at 6 ms (T_{ON}), 21 ms (T_{OFF}) and various I_P: (a–d) without additives, (e–h) with 0.5 g l^{-1} PVA, (I–l) with 0.5 g l^{-1} PVA + 0.2 g l^{-1} PIP; (a, e, and i) 5 A dm^{-2}; (b, f, and j) 7 A dm^{-2}; (c, g, and k) 9 A dm^{-2}; (d, h, and l) 11 A dm^{-2}.

36.48° to 36.36°, indicating deformation of Zn–Co alloy crystal lattices.

3.3.2. T_{ON} effect

Fig. 11 depicts the effect of T_{ON} at constant T_{OFF} (21 ms) and I_P (5 A dm^{-2}) on the lattice orientations of Zn–Co deposits. The sharp peaks confirm the microcrystalline morphology. A decrease in the intensity of the peaks associated with planes [00.2], [10.3] and [11.0] and corresponding increase in the intensity of the cobalt oxide, cobalt hydroxide and low angle pyramidal [10.1] peaks of the zinc-rich (η-phase) were observed, when T_{ON} increased from 9 to 15 ms. This might be due to the

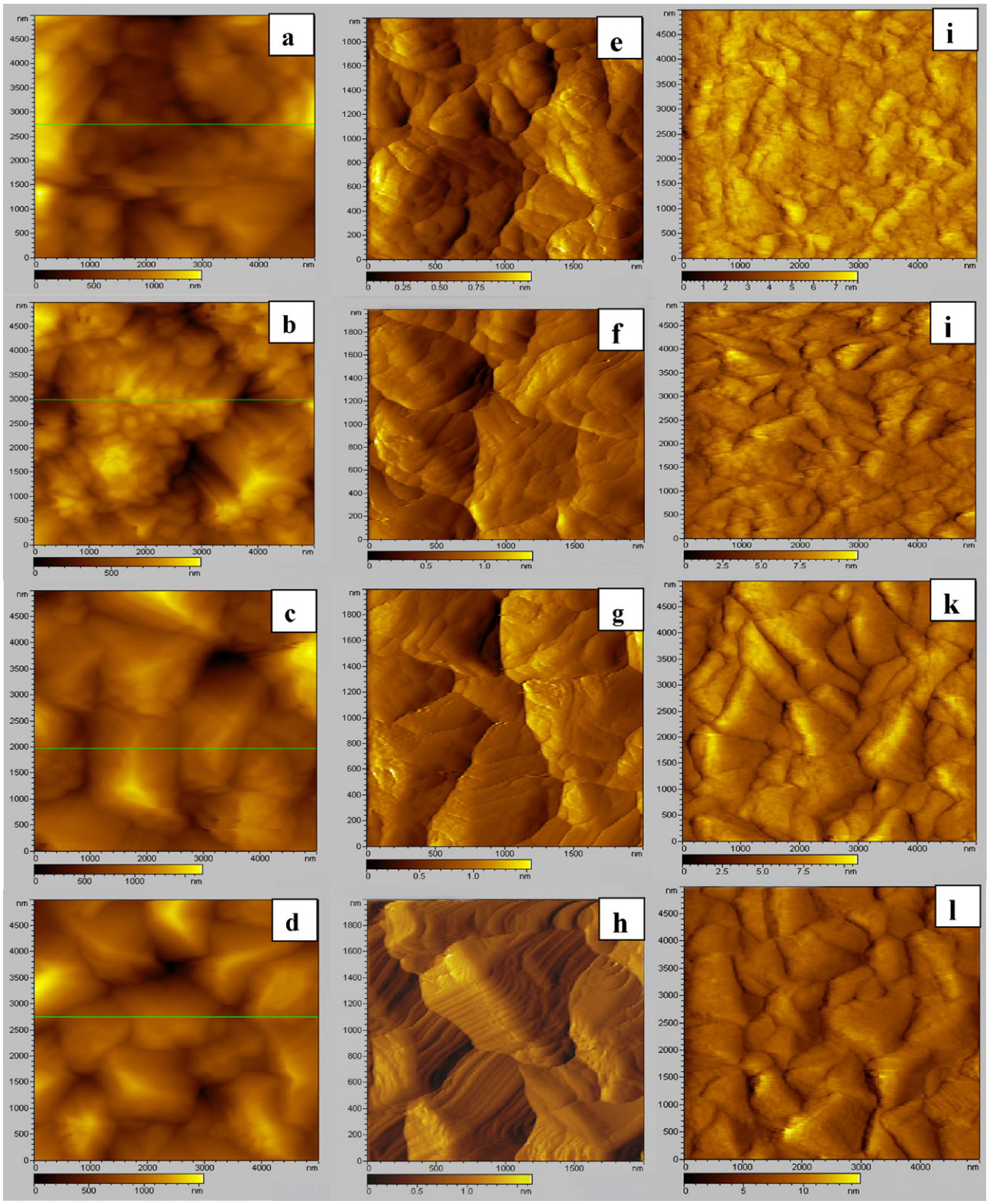

Fig. 8. AFM images of zinc–cobalt deposits obtained at 6 ms (T_{ON}), 21 ms (T_{OFF}) and various I_P: (a–d) without additives, (e–h) with 0.5 g l^{-1} PVA, (I–l) with 0.5 g l^{-1} PVA + 0.2 g l^{-1} PIP. (a, e, and i) 5 Adm^{-2}; (b, f, and j) 7 Adm^{-2}; (c, g, and k) 9 Adm^{-2}; (d, h, and l) 11 Adm^{-2}.

lower inclusion of cobalt content in the deposit at higher T_{ON} [9].

3.3.3. I_P effect

3.3.3.1. Without additive. Fig. 12 explicitly shows the different orientations obtained by variations of I_P at constant T_{OFF} (21 ms) and T_{ON} (6 ms). The intensity of the peaks associated with [00.2], [10.2] and [10.3] diminished with increased I_P. This may be attributed to the cobalt inclusion in the deposits. At higher I_P values, the peak [10.0] of prismatic plane shifts from 39.3° to 38.9° (2θ values). The peak [10.1] corresponding to the high angle pyramidal plane of the zinc-rich η-phase dominates at higher I_P. No significant RTC value

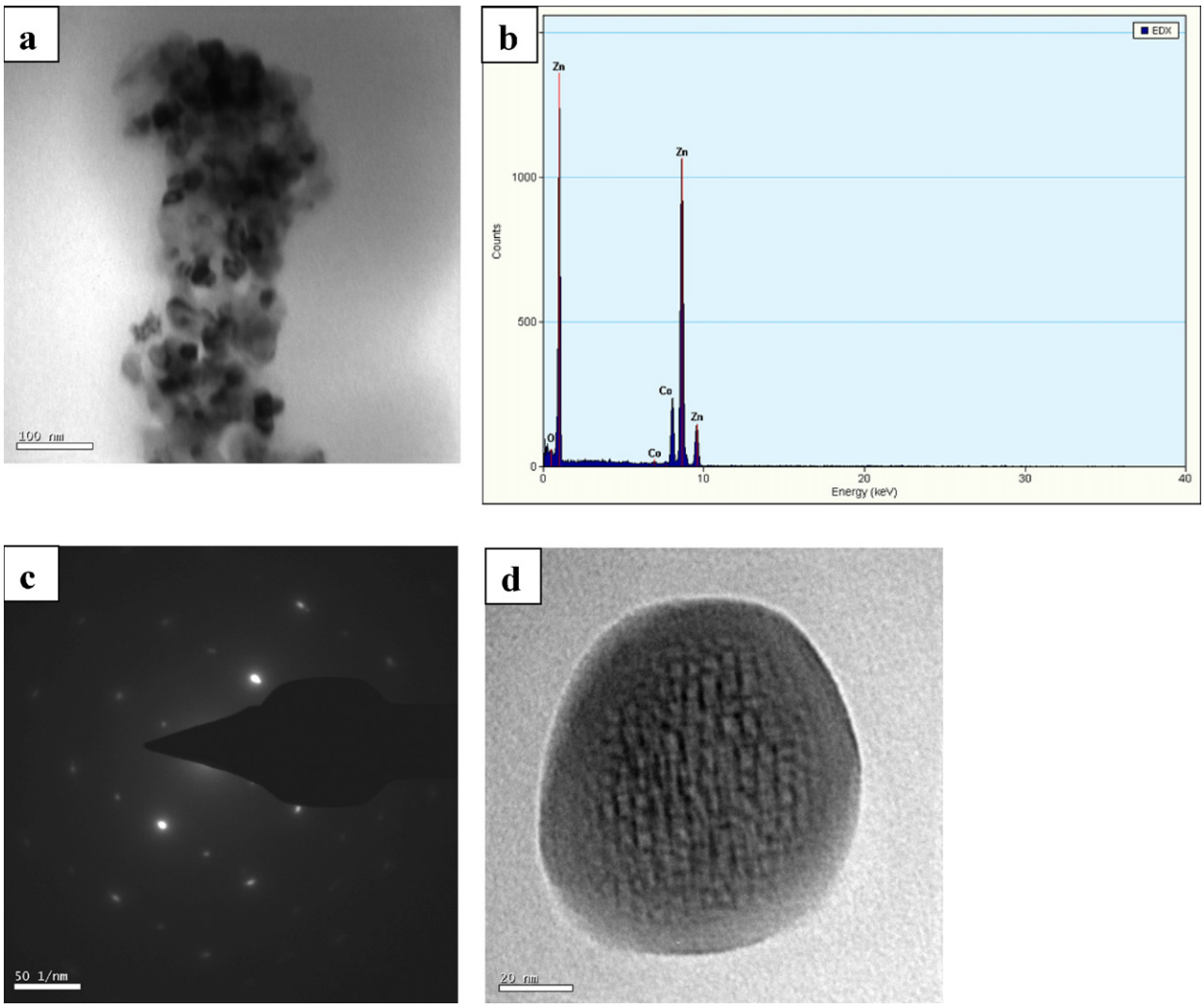

Fig. 9. TEM images of Zn–Co deposits at 6 ms (T_{ON}), 21 ms (T_{OFF}), 7 Adm^{-2}, with 0.5 g l^{-1} PVA + 0.2 g l^{-1} PIP. (a) Grain distribution; (b) EDX pattern; (c) selected area diffraction pattern; (d) microcrystalline view.

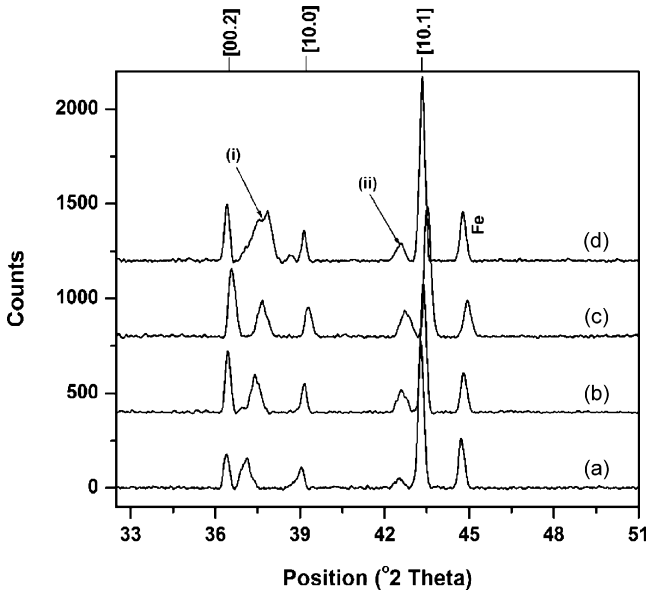

Fig. 10. XRD patterns of zinc–cobalt deposits at 6 ms (T_{ON}), 5 Adm^{-2} (I_P) and various OFF-time (T_{OFF}) of (a) 6 ms, (b) 21 ms, (c) 30 ms, (d) 60.7 ms.

could be observed in the absence of additives (Table 1). Nevertheless, 17.2, 20.9 and 39.9% of crystallites oriented to the [10.1], [11.0] and [11.2], respectively.

3.3.3.2. With PVA. The intensity of the peaks [00.2], [10.0], [10.3] and [11.0] diminished while the prismatic peak [10.1] corresponding to zinc-rich η-phase, cubic Co_5Zn_{21} [58] and cobalt hydroxide increased with I_P up to 9 Adm^{-2} in the bath containing 0.5 g l^{-1} PVA (Fig. 13). The peaks [10.2] and [11.0] showed slight deflections. Presence of PVA showed a pseudo-texture (Table 1). 37.6 and 43.7% of crystallites oriented to the [11.2], [10.1], respectively.

3.3.3.3. With PVA and PIP. The intensity of peaks corresponding to [00.2], [10.2], [10.3] and Co_5Zn_{21} diminished while the high angle pyramidal plane [10.1] associated with zinc-rich η-phase dominates at higher I_P and prismatic plane [10.0] persist up to 7 Adm^{-2} and then decreases gradually (Fig. 14). From Table 1, in the presence of PVA and PIP, 69.1% of crystallites are orientated parallel to the [10.1] crystallographic plane. This indicates that in the presence of additives, [10.1] is the preferred crystallographic orientation. This might be due to the fact that additives adsorbs onto the growing deposit. This affects the electrocrystallization process with a consequence to alter the texture of the deposits.

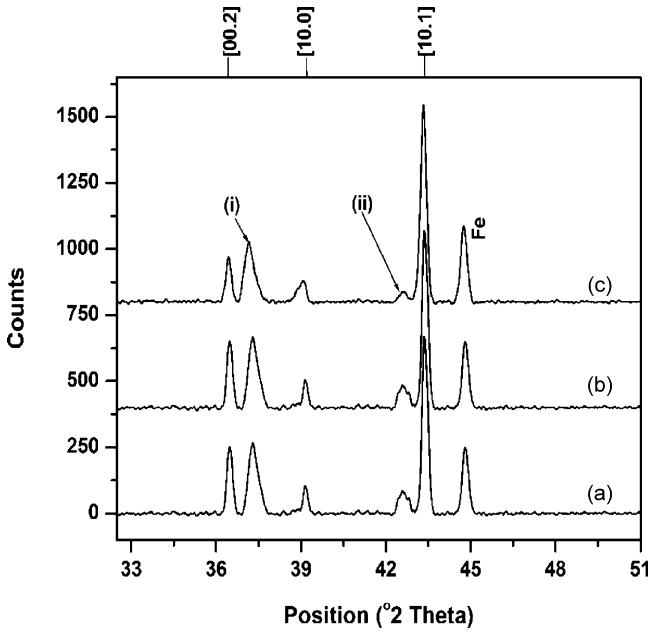

Fig. 11. XRD patterns of zinc–cobalt deposits at 21 ms (T_{OFF}), 5 Adm^{-2} (I_P) and various ON-time (T_{ON}) of (a) 9 ms, (b) 12 ms, (c) 15 ms.

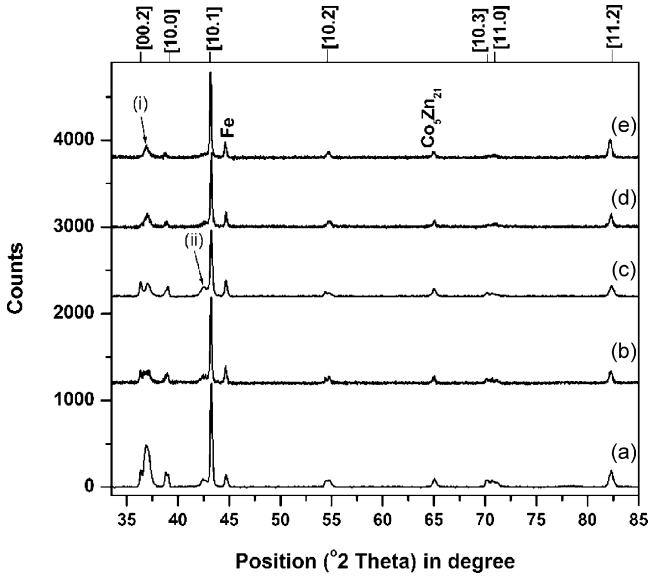

Fig. 12. XRD patterns of zinc–cobalt deposits at 6 ms (T_{ON}), 21 ms (T_{OFF}) and various peak current density (I_P) of (a) 5 Adm^{-2}, (b) 7 Adm^{-2}, (c) 9 Adm^{-2}, (d) 11 Adm^{-2}, (e) 13 Adm^{-2}.

Table 1
Relative texture co-efficient (RTC in %) of Zn–Co alloy.

(hkl)	I_P (at 7 Adm^{-2})		
	Without additive	With PVA	With PVA and PIP
00.2	6.67	3.95	6.5
10.0	8.3	2.8	9.0
10.1	17.2	43.7	69.1
10.2	7.1	2.9	1.5
11.0	20.9	9.1	4.9
11.2	39.9	37.6	9

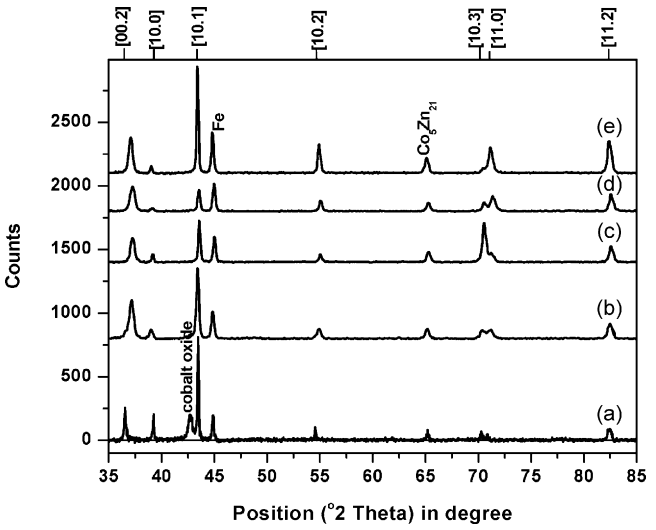

Fig. 13. XRD patterns of zinc–cobalt deposits at 6 ms (T_{ON}), 21 ms (T_{OFF}), 0.5 g l^{-1} PVA and various peak current density (I_P) of (a) 5 Adm^{-2}, (b) 7 Adm^{-2}, (c) 9 Adm^{-2}, (d) 11 Adm^{-2}, (e) 13 Adm^{-2}.

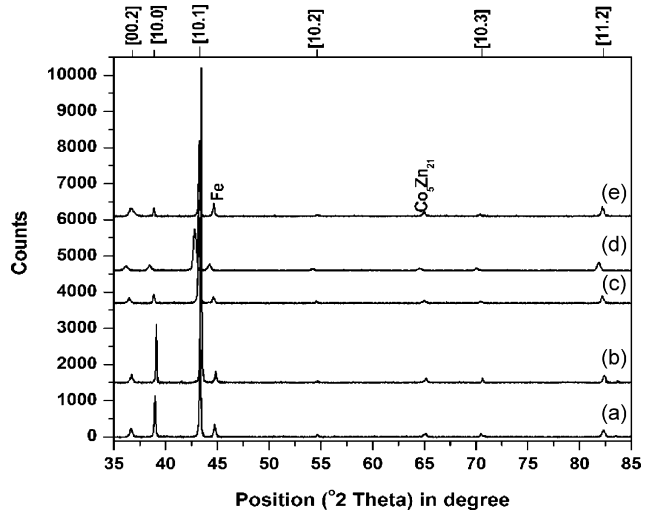

Fig. 14. XRD patterns of zinc–cobalt deposits at 6 ms (T_{ON}), 21 ms (T_{OFF}), 0.5 g l^{-1} PVA, 0.2 g l^{-1} PIP and various peak current density (I_P) of (a) 5 Adm^{-2}, (b) 7 Adm^{-2}, (c) 9 Adm^{-2}, (d) 11 Adm^{-2}, (e) 13 Adm^{-2}.

4. Conclusion

Adherent and bright microcrystalline Zn–Co deposits containing grain size ranging from 40 to 45 nm were produced from an alkaline non-cyanide electrolyte with additives. Increasing T_{ON}, increases micro-cluster with decreased cobalt content in the deposits while vice-versa with increasing T_{OFF}. Grain refinement was also observed by increasing I_P. Microcrystalline deposit containing 0.68–0.7 wt.% Co having [10.1] as preferred orientation was produced at 6 ms (T_{ON}), 21 ms (T_{OFF}) and 7 Adm^{-2} from electrolyte containing additives. The advantages of pulse electrodeposition from this study includes (1) less wt.% Co electrolyte sufficient to obtain required cobalt content, (2) an agent for effective grain refinement, at moderate current densities of deposition, enabling the preparation of compact, (3) 50% less additive concentration is sufficient to obtain high quality deposit as compared to DC [41]. The new bath also has the additional advantage of being eco-friendly in that it uses only easily disposable organics.

Acknowledgements

The authors wish to express their sincere thanks to the Director, CECRI for the encouragement given and permission to publish this paper. Thanks are also due to the staffs of Central Instrumentation facility for the support rendered. M.S. Chandrasekar expresses his thanks to CSIR, New Delhi for financial support under CSIR Diamond Jubilee Research Intern Scheme.

References

[1] A. Brenner, Electrodeposition of Alloys: Principles and Practice, vol. I–II, Academic Press, New York, 1963.
[2] E. Gomez, X. Alcobe, E. Valles, J. Electroanal. Chem. 505 (2001) 54.
[3] R. Ramanauskas, P. Quintana, L. Maldonado, R. Pomes, M.A. Pech-Canul, Surf. Coat. Technol. 92 (1997) 16.
[4] M.A. Pech-Canul, R. Ramanauskas, L. Maldonado, Electrochim. Acta 42 (1997) 255.
[5] R. Ramanauskas, L. Muieshkova, L. Maldonado, P. Dobrovolskis, Corros. Sci. 40 (1998) 402.
[6] S.W. Pagotto Jr., C.M.A. Freire, M. Ballester, Surf. Coat. Technol. 122 (1999) 10.
[7] E.O.S. Carpenter, J.P.G. Farr, Trans. Inst. Met. Finish. 76 (1998) 135.
[8] T. Tsuru, S. Kobayshi, T. Akiyama, H. Fukushima, S.K. Gogia, R. Kammel, J. Appl. Electrochem. 27 (1997) 209.
[9] J. Mahieu, K. De Wit, A. De Boeck, B.C. De Cooman, J. Mater. Eng. Perform. 8 (1999) 561.
[10] D. Koleva, N. Boshkov, G. Raicheski, L. Veleva, Trans. Inst. Met. Finish. 83 (2005) 188.
[11] A. Cunha, S.D. Carpenter, J.Z. Ferreira, D.E.O.S. Carpenter, J.P.G. Farr, Corros. Eng. Sci. Technol. 38 (2003) 313.
[12] J.B. Bajat, V.B. Miskovic-Stankovic, M.V. Maksimovic, Electrochim. Acta 47 (2002) 4101.
[13] Shanmugasigamani, Malathy Pushpavanam, Trans. Inst. Met. Finish. 86 (2008) 122.
[14] R. Ramanauskas, Appl. Surf. Sci. 153 (1999) 53.
[15] R. Ramanauskas, R. Juskenas, A. Kalinicenko, L.F. Garfias-Mesias, J. Solid State Electrochem. 8 (2004) 416.
[16] R. Fratesi, G. Roventi, G. Giuliani, C.R. Tomachuk, J. Appl. Electrochem. 27 (1997) 1088.
[17] S. Rajendran, S. Bharathi, C. Krishna, T. Vasudevan, Plat. Surf. Finish. 84 (1997) 53.
[18] A.P. Shears, Trans. Inst. Met. Finish. 67 (1989) 67.
[19] P.D.L. Neto, A.N. Correia, R.P. Colares, J. Brazilian Chem. Soc. (2007).
[20] R. Frateri, Surf. Coat. Technol. 63 (1994) 97.
[21] Zn-Co: Fighting Corros. In the 90's, Prod. Finish. 54 (1990) 38.
[22] N.R. Short, S. Zhou, J.K. Dennis, Surf. Coat. Technol. 79 (1996) 218.
[23] C.R. Tomachuk, C.M. de, A. Freire, M. Ballester, R. Fratesi, G. Roventi, Surf. Coat. Technol. 122 (1999) 6.
[24] M.S. Chandrasekar, Shanmugasigamani, Malathy Pushpavanam, J. Solid State Electrochem. 13 (2009) 781.
[25] Z.-M. Tu, J.-S. Zhang, W.L. Li, Z.-L. Yang, M.Z. An, Trans. Inst. Met. Finish. 73 (1995) 48.
[26] P.Y. Chen, I.W. Sun, Electrochim. Acta 46 (2001) 1169.
[27] R. Ramanauskas, L. Gudaviciute, A. Kalinicenko, R. Juskenas, J. Solid State Electrochem. 9 (2005) 900.
[28] P.L. Cavallotti, A. Vicenzo, M. Bestetti, S. Franz, Surf. Coat. Technol. 169 (2003) 76.
[29] Z.A. Hamid, Mater. Lett. 57 (2003) 2558.
[30] G.D. Wilcox, D.R. Gabe, Corros. Sci. 35 (1993) 1251.
[31] H. Dahms, I.M. Croll, J. Electrochem. Soc. 112 (1965) 771.
[32] M. Yunus, C. Capel-Boute, C. Decroly, Electrochim. Acta 10 (1965) 885.
[33] J. Mindowicz, C. Capel-Boute, C. Decroly, Electrochim. Acta 10 (1965) 91.
[34] K. Higashi, H. Fukushima, T. Urakawa, T. Adaniya, K. Matsudo, J. Electrochem. Soc. 128 (1981 2081).
[35] H. Fukushima, T. Akiyama, K. Higashi, R. Kammel, M. Karimkhani, Metall 44 (1990) 754.
[36] E. Gomez, E. Valles, J. Electroanal. Chem. 397 (1995) 177.
[37] E. Chassaing, R. Wiart, Electrochim. Acta 37 (3) (1992) 545.
[38] M.E. Bahrololoom, D.R. Gabe, G.D. Wilcox, J. Electrochem. Soc. 150 (3) (2003) C144.
[39] M.S. Chandrasekar, Malathy Pushpavanam, Electrochim. Acta 53 (2008) 3313.
[40] M.S. Chandrasekar, Shanmugasigamani, Malathy Pushpavanam, J. Appl. Electrochem., submitted for publication.
[41] Shanmugasigamani, Malathy Pushpavanam, Trans. Inst. Met. Finish. 84 (2006) 326.
[42] H. Geduld, Alkaline Non-cyanide Zinc Plating in Zinc Plating, ASM International Metals Park, OH, 1988, p. 60.
[43] E. Budman, Met. Finish. 93 (1995) 60.
[44] B.D. Cullity, Elements of X-ray Diffraction, 2nd edn., Addison-Wesley, Philippines, 1978.
[45] A. Stankeviciute, K. Leinartas, G. Bikulcius, D. Virbalyte, A. Sudavicius, E. Juzeliunas, J. Appl. Electrochem. 28 (1998) 89.
[46] N. Ibl, J.Cl. Puippe, H. Angerer, Surf. Technol. 6 (1978) 287.
[47] J. Puippe, F. Leaman, Theory, Practice of Pulse Plating, AESF Publication, Orlando, 1986.
[48] E. Gomez, X. Alcobe, E. Valles, J. Electrochem. Soc. 142 (1995) 4091.
[49] C.C. Youssef, P.S. Koch, Fedkiw, J. Electrochem. Soc. 151 (2004) 103.
[50] J.P. Celis, M. De Bonte, J.R. Roos, Trans. Inst. Met. Finish. 72 (1994) 89.
[51] R.T.C. Choo, J.M. Toguri, A.M. El-Sherik, U. Erb, J. Appl. Electrochem. 25 (1995) 384.
[52] M. Mouanga, L. Ricq, P. Bercot, Surf. Coat. Technol 202 (2008) 1645.
[53] L.Ph. Berube, G. L'Esperance, J. Eelectrochem. Soc. 136 (1989) 2314.
[54] Powder Diffraction File, Inorganic Volume PD/S 5iRB, American Society for Testing and Materials, USA, 1969.
[55] J.L. Ortiz-Aparicio, Y. Meas, G. Trejo, R. Ortega, T.W. Chapmana, E. Chainet, P. Ozil, Electrochim. Acta 52 (2007) 4742.
[56] N.A. Pangarov, J. Electroanal. Chem. 9 (1965) 70.
[57] D. Vasilakopoulos, M. Bouroushian, N. Spyrellis, Trans. Inst. Met. Finish. 79 (2001) 107.
[58] S.M. Rashwan, A.E. Mohamed, S.M. Abdel-Wahaab, M.M. Kamel, J. Appl. Electrochem. 33 (2003) 1035.